NJC

LETTER

CrossMark
← click for updates

Green catalyst: magnetic La$_{0.7}$Sr$_{0.3}$MnO$_3$ hollow microspheres†

Cuiping Zhou,[a] Keke Huang,[a] Long Yuan,[a] Wenchun Feng,[b] Xuefeng Chu,[c] Zhibin Geng,[a] Xiaofeng Wu,[a] Liying Wang[a] and Shouhua Feng*[a]

Recently, the development of recyclable, stable, highly efficient water-splitting catalysts is urgent. Herein, we report magnetic La$_{0.7}$Sr$_{0.3}$MnO$_3$ hollow microspheres, which show high activity, stability and long lifetime for photocatalytic water oxidation at room temperature. Our design route for this green catalyst may be applied to other environmental- and energy-related technological aspects.

The design and development of green catalysts for energy and environmental applications are desirable due to their recyclability after catalytic reactions. Sustainable and green catalysts are usually regarded as specific features, such as efficient recovery, good recyclability, low preparation cost, and high activity and stability.[1] Among various non-noble metal catalysts, perovskite oxides are one type of promising structure due to their chemical and thermal stability and the easy tailoring method over their size, shape, composition and electronic state.[2] Although there are many previous reports concentrating on the preparation and catalytic behavior of perovskite oxides, there are comparatively few reports for ferromagnetic perovskite catalysts.[3] Co- and Mn-based perovskites are mainly desired as substitutes of noble metals for heterogeneous catalysis, particularly in CH$_4$, CO, and NO$_x$ oxidation.[4] La$_{1-x}$Sr$_x$MnO$_3$, a typical perovskite manganese oxide with a stable structure, not only has a high Curie temperature (T_C) and magnetic moment at room temperature, but also exhibits good performance in catalysis.[5–7] Therefore, the La$_{1-x}$Sr$_x$MnO$_3$ is a good choice as a prospective green catalyst for environmental benefit.

[a] *State Key Laboratory of Inorganic Synthesis and Preparative Chemistry, College of Chemistry, Jilin University, Changchun 130012, P. R. China. E-mail: shfeng@jlu.edu.cn; Fax: +86-431-85168624; Tel: +86-431-85168661*

[b] *Department of Chemistry and Chemical Biology, Rutgers University, Piscataway, New Jersey 08854, USA*

[c] *Department of Basic Science, Jilin Jianzhu University, Changchun 130118, P. R. China*

Hollow micro-/nanostructures have been highly attractive in biomedical engineering, energy storage, sensing and particularly in catalysis due to their lower density, highly active area and characteristic void space for matter and energy exchange (*e.g.* capture photon).[8–11] To date, there have been many effective methods for preparing hollow spheres based on hard, soft template and template-free strategies.[12] During the past decades, electrospinning has been widely used for fabricating nanofibers[13,14] because it is cost effective, environmentally friendly[15] and simple to control the surface morphology.[16,17] By reducing the precursor sol viscosity, hollow spheres can be obtained *via* subsequent calcination.

In our previous work, we found that catalytic behavior in the oxidation of CO and CH$_4$ depended on surface ratio of Mn^{3+}/Mn^{4+} of LSMO prepared *via* different methods.[18] By engineering surface structures and oxygen species of LSMO, more B-sites on the terminated perovskite improve catalytic activity toward CO.[19] Recently, we found non-spherical field ions on the shape modulation of hydrothermally prepared LSMO crystals.[20] In this communication, La$_{1-x}$Sr$_x$MnO$_3$ hollow microspheres were prepared by a general electrospinning method with minor modification. It shows high activity, stability and longer catalyst lifetime for photocatalytic water oxidation in comparison with nanoparticles prepared by conventional sol–gel.

Fig. 1 presents typical SEM and TEM images of LSMO microspheres prepared by electrospinning followed by calcination at various rates. They clearly show the change in morphology with increasing heating rate. Calcined at 1 °C min^{-1}, the surface of spheres was smooth and the thickness was about 0.8 µm. When the rate was 5 °C min^{-1}, their surface intensely shrank and the thickness of spheres became considerably thinner at around 0.3 µm. Upon further increasing the rate to 10 °C min^{-1}, the LSMO spheres possessing smooth surface and ultrathin shell were finally obtained.

XRD patterns (Fig. S1a, ESI†) indicate a hexagonal phase feature with space group $R\bar{3}c$, and all characteristic diffraction peaks match well with the document (JCPDS No. 51-0409). Inductively coupled plasma spectroscopy (ICP) indicates that

Fig. 1 SEM-TEM images of $La_{0.7}Sr_{0.3}MnO_3$ microspheres calcined at the heating rate of (a and b) 1 °C min^{-1}, (c and d) 5 °C min^{-1}, and (e and f) 10 °C min^{-1} under 650 °C for 5 h (denoted as LSMO-1, LSMO-5 and LSMO-10, respectively). Scale bar: 5 μm in SEM images.

the composition of the products is $La_{0.7}Sr_{0.3}MnO_3$. The high-resolution transmission electron microscopy (HRTEM) image (Fig. S1b, ESI†) of the LSMO-10 hollow spheres displays that the distance of the adjacent atomic lattice fringes is 0.38 nm, which is consistent with the (012) plane of its hexagonal phase.

To explore the mechanism of formation, several parallel experiments were carried out. Based on their results, the mechanism involving Ostwald ripening is proposed (Fig. 2). In precursor sol, the inorganic salts are well dispersed along with long soft chains of PVP with many polar groups. In the electrospinning process, as a result of low viscosity, the surface tension has a dominant influence, and the liquid jet prefers to shrink to a spherical droplet to acquire the smallest surface area.[21] In the subsequent calcination process, precursor spheres will undergo the removal of polymer, the decomposition of inorganics and the crystallization and Ostwald ripening (larger crystallites grow at the cost of the smaller ones). Compared with crystallites in the outer surfaces, those located in the inner cores have higher surface energies (ascribed to the imaginary smaller sphere with a higher curvature) and are considerably easier to be dissolved.[22] On the premise of limited calcination time, lower calcination temperature
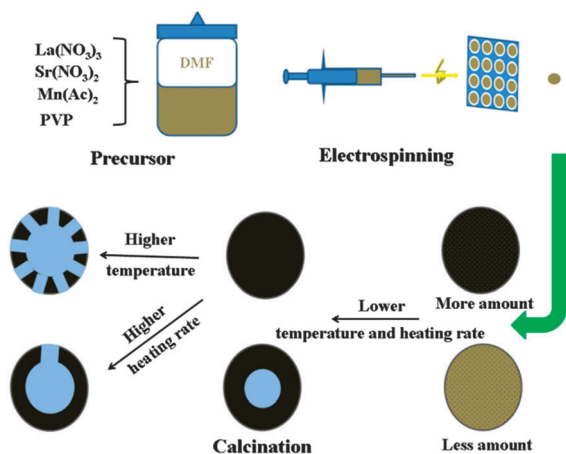
and heating rate tend to slow the process of the dissolution and recrystallization. The dense precursor spheres (Fig. S2, ESI†) with more inorganics will be solid spheres for the negligible ripening effect, whereas their hollowing effect can be evidently observed in the loose ones of less inorganics (Fig. S3, ESI†). However, if the calcination temperature and heating rate increase, the process of the dissolution and recrystallization is violent, resulting in the solid spheres turning into hollow spheres (Fig. S4, ESI† and Fig. 1). The release of gas produced from the decomposition of PVP and inorganics is also responsible for this hollowing process, confirmed by the pores on hollow spheres.

In order to further verify our assumption of the mechanism of formation of hollow spheres, time-dependent experiments were also carried out. Compared with the LSMO-1 calcined for 5 h (Fig. 1a), an evident crack appeared, and the hollow interior with a shell thickness of about 0.3 μm was observed from high-magnification images (Fig. S5a, ESI†) after calcination for 7 h. By further increasing the time to 10 h, the shell thickness of the hollow sphere (Fig. S5b, ESI†) evidently grew much thinner, and many pores appeared on the surfaces of spheres due to the long enough ripening process. The increase in interior-cavity size with increasing the calcination time is consistent with our propositional Ostwald ripening mechanism.

For studying the catalytic difference between LSMO hollow microspheres prepared by electrospinning and LSMO nanoparticles (Fig. S6, ESI†) prepared by direct sol–gel, the photocatalytic water oxidation was performed in a bicarbonate buffer solution (1 mM, 20 mL, pH 7.0) containing a 250 ppm catalyst, $Na_2S_2O_8$ (10 mM) as a two-electron oxidant and $[Ru(bpy)_3]^{2+}$ (0.5 mM) as a photosensitizer. Their time courses of O_2 evolution are shown in Fig. 3. No O_2 evolution was confirmed from a reaction solution without the catalyst. As shown in Fig. 3a and b, the O_2 evolution rates with LSMO-1 and LSMO-5 were both larger
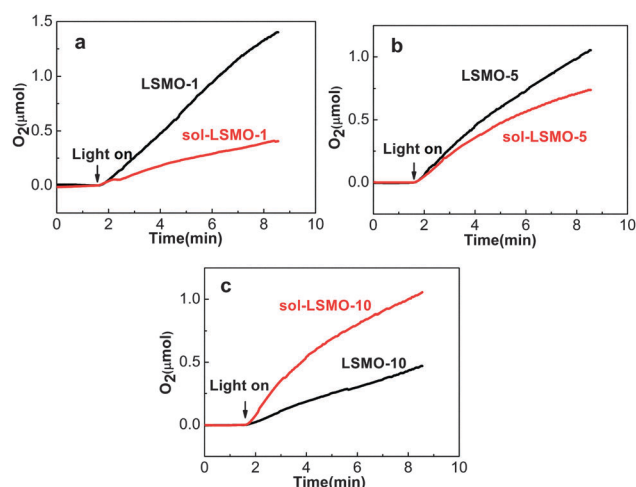

Fig. 2 Schematic illustration of the proposed formation process of the hollow spheres.

Fig. 3 Time courses of O_2 evolution with (a) LSMO-1 and sol–LSMO-1, (b) LSMO-5 and sol–LSMO-5, (c) LSMO-10 and sol–LSMO-10 under visible-light irradiation (a Newport oriel sol3A solar simulator through a transmitting glass filter, $\lambda > 420$ nm) of a bicarbonate buffer solution (1 mM, 20 mL, pH 7.0) containing $[Ru(bpy)_3]^{2+}$ (0.5 mM), $Na_2S_2O_8$ (10 mM) with 250 ppm catalyst [electrospun LSMO microspheres and LSMO nanoparticles prepared by direct sol–gel (denoted as sol–LSMO)].

than their corresponding sol–LSMO-1 and sol–LSMO-5, respectively, particularly for LSMO-1. Although the R_{O_2} of LSMO-10 was lower than that of sol–LSMO-10, the approximately constant R_{O_2} indicates that it has the longer catalyst lifetime in contrast with sol–LSMO-10 (Fig. 3c); this advantage, which is important for catalyst, applies to all of the LSMO microspheres prepared by electrospinning. According to the overall photocatalytic cycle of water oxidation with $Na_2S_2O_8$, $[Ru(bpy)_3]^{2+}$ and water oxidation catalysts (WOCs)[23] and that catalyst lifetime is mainly associated with its active surface area under suitable conditions,[24] we speculate that the longer lifetime might be attributed to the spherical structure for facilitating the desorption of inactivated photosensitizers, which is beneficial for the reabsorption of active photosensitizers and maintaining stable catalytic efficiency.

To gain insight into the factors responsible for the high water oxidation activity of LSMO-1 and LSMO-5, they were further investigated by XPS and nitrogen adsorption–desorption measurements. For LSMO-X microspheres and corresponding sol–LSMO-X nanoparticles, they were prepared from the same sol undergoing the same calcination process. Fig. 4 displays the XPS spectrum for the Mn 2p energy region of LSMO and sol–LSMO. From Fig. 4a and Table S1 (ESI†), we observe that the binding energy and content of Mn in the surface of LSMO-1 is almost the same as that of sol–LSMO-1, but the BET specific surface area (Table S2, ESI†) of LSMO-1 (11.1644 m^2 g^{-1}) is considerably lower than that of sol–LSMO-1 (16.9738 m^2 g^{-1}), which leads to the decrease in surface reaction sites. However, to our surprise, the LSMO-1 has considerably higher O_2 evolution rates than sol–LSMO-1 in a photocatalytic water oxidation test. We deduce that it is mainly ascribed to the spherical structure. Magnetically stirred in a reaction solution, microspheres are considerably easier to maintain optimally disperse states than nanoparticles, and thus efficiently contact with the photosensitizer and H_2O molecules, making the photocatalytic process more efficient.[25] Compared with LSMO-1, the water oxidation activity of LSMO-5 is not much higher than that of sol–LSMO-5, although LSMO-5 possesses much higher content

of surface Mn. The reason is likely for the decreased crystallinity[26] (Fig. S1a, ESI†) and relatively imperfect structure. As to the phenomenon that the R_{O_2} of LSMO-10 is lower than that of sol–LSMO-10, we think it is a result of the comprehensive effect of its decreased content of Mn, higher binding energy, which indicates a decreased ratio of Mn^{3+} (served as active site) to Mn^{4+},[27] much lower BET surface area and fragile structure (Fig. 1e) than sol–LSMO-10. Although LSMO-1, LSMO-5 and LSMO-10 do not show consistent trends in water oxidation activity, it gives us an idea that we can control the calcination process to obtain higher catalytically active desirable products.

In addition, we can easily collect them from the solution after the reaction because of their strong ferromagnetism at room temperature (inset in the upper left of Fig. 5), and the stability is fine (Fig. S7, ESI†). The zero-field-cooled (ZFC) and field-cooled (FC) magnetization plots of LSMO-1, LSMO-5 and LSMO-10 are presented in Fig. S8 (ESI†). Shown in these plots, obvious transitions from ferromagnetism to paramagnetism are observed at around 357 K for LSMO-1 and at about 337 K for LSMO-5 and LSMO-10. Their M–H curves (Fig. 5) are clearly irreversible (inset in the lower right corner of Fig. 5), which is consistent with the room-temperature ferromagnetism due to the double exchange between Mn^{3+} and Mn^{4+}.[28]

Their coercive field, remanent magnetization and saturated magnetization values are summarized in Table S3 (ESI†). Their remanent magnetization (M_R) values are similar. However, the saturation magnetization (M_S) of LSMO-1 and LSMO-10 is considerably higher than that of LSMO-5, whereas opposite change is observed in coercivity (H_C). We propose that it is mainly related to the surface anisotropy.[29] Compared with the rough surface, the smooth surface enables the surface metal atom to possess a more symmetric coordination and smaller degree of spin disorder and pinning. Compared with hollow spheres with small interior-cavity size, those having large ones induce the spin disorder and pinning for less symmetric coordination. The H_C is proportional to the surface anisotropy, whereas the M_S is inverse. As shown in Fig. 1, the order of their interior-cavity size is LSMO-1 < LSMO-5 < LSMO-10, which indicates that the H_C values should be increasing. However, the coercivity values of
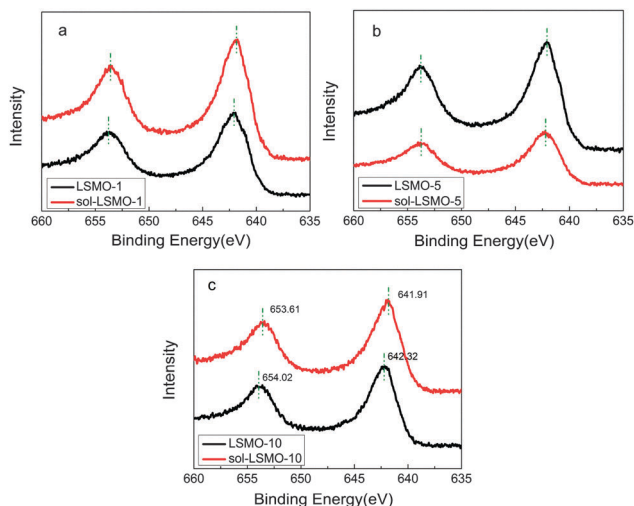

Fig. 4 XPS spectra in the Mn 2p energy region of $La_{0.7}Sr_{0.3}MnO_3$ prepared by electrospinning and direct sol–gel method, respectively.
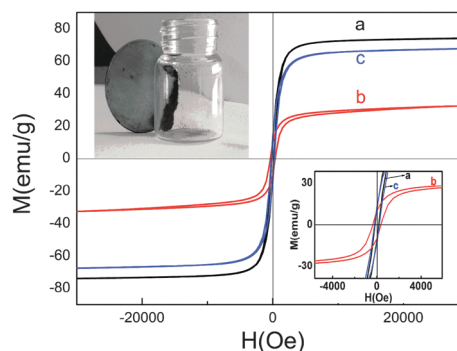

Fig. 5 Field dependence of the magnetization curves (at 4 K) of (a) LSMO-1, (b) LSMO-5 and (c) LSMO-10 (the inset in the upper left is a picture of LSMO-1 and a magnet, and the inset in the lower right corner is enlarged M–H curves).

LSMO-1 and LSMO-10, which possess smoother surfaces, are both considerably lower than that of LSMO-5, indicating that the surface has a dominant effect on the coercivity and saturation magnetization. This discovery helps us to have a good understanding of the relationship between magnetic property and morphology such that we can greatly satisfy the requirements of applications in catalysis by controlling M_S of LSMO.

In conclusion, the magnetic perovskite $La_{0.7}Sr_{0.3}MnO_3$ hollow spheres have been prepared by controlling the calcination process of the electrospun precursor. The rugged spherical structure causes $La_{0.7}Sr_{0.3}MnO_3$ microspheres to exhibit high activity, stability and longer lifetime in photocatalytic water oxidation, and they could be easily recycled after catalytic reactions. The strategy is important to other environmental and energy applications.

Experimental

Preparation of LSMO hollow spheres: In a typical experiment, 4 mmol stoichiometric amount of $La(NO_3)_3 \cdot 6H_2O$, $Sr(NO_3)_2$, $Mn(CH_3COO)_2 \cdot 4H_2O$ and 1.5381 g polyvinylpyrrolidone (PVP) were mixed in 5 mL N,N-dimethylformamide (DMF) and stirred. The final homogeneous mixture was loaded into a plastic syringe. The applied voltage was 15 kV at a constant distance of 13 cm between the tip and collector under a flow rate of 0.15 mL h^{-1} with a needle of 0.34 mm inner diameter. The obtained LSMO–PVP composites were dried at 60 °C for 12 h and calcined at 1 °C min^{-1}, 5 °C min^{-1} and 10 °C min^{-1} under 650 °C for 5 h in air.

Notes and references

1 D. Wang and D. Astruc, *Chem. Rev.*, 2014, **114**, 6949–6985.
2 S. Royer, D. Duprez, F. Can, X. Courtois, C. Batiot-Dupeyrat, S. Laassiri and H. Alamdari, *Chem. Rev.*, 2014, **114**, 10292–10368.
3 A. Aguadero, H. Falcon, J. M. Campos-Martin, S. M. Al-Zahrani, J. L. G. Fierro and J. A. Alonso, *Angew. Chem.*, 2011, **123**, 6687–6691.
4 C. H. Kim, G. S. Qi, K. Dahlberg and W. Li, *Science*, 2010, **327**, 1624–1627.
5 Y. Tokura, *Rep. Prog. Phys.*, 2006, **69**, 797–851.
6 H. Arandiyan, H. X. Dai, J. G. Deng, Y. X. Liu, B. Y. Bai, Y. Wang, X. W. Li, S. H. Xie and J. H. Li, *J. Catal.*, 2013, **307**, 327–339.
7 S. H. Liang, F. Teng, G. Bulgan and Y. F. Zhu, *J. Phys. Chem. C*, 2007, **111**, 16742–16749.
8 X. Y. Lai, J. E. Halpert and D. Wang, *Energy Environ. Sci.*, 2012, **5**, 5604–5618.
9 X. W. Lou, L. A. Archer and Z. C. Yang, *Adv. Mater.*, 2008, **20**, 3987–4019.
10 Y. Zhao and L. Jiang, *Adv. Mater.*, 2009, **21**, 3621–3638.
11 C. Q. Zhu, B. G. Lu, Q. Su, E. Q. Xie and W. Lan, *Nanoscale*, 2012, **4**, 3060–3064.
12 J. Hu, M. Chen, X. S. Fang and L. M. Wu, *Chem. Soc. Rev.*, 2011, **40**, 5472–5491.
13 A. Greiner and J. H. Wendorff, *Angew. Chem., Int. Ed.*, 2007, **46**, 5670–5703.
14 X. F. Lu, C. Wang and Y. Wei, *Small*, 2009, **5**, 2349–2370.
15 V. Thavasi, G. Singh and S. Ramakrishna, *Energy Environ. Sci.*, 2008, **1**, 205–221.
16 D. Li and Y. N. Xia, *Adv. Mater.*, 2004, **16**, 1151–1170.
17 C. L. Zhang and S. H. Yu, *Chem. Soc. Rev.*, 2014, **43**, 4423–4448.
18 K. K. Huang, X. F. Chu, W. C. Feng, C. P. Zhou, W. Z. Si, X. F. Wu, L. Yuan and S. H. Feng, *Chem. Eng. J.*, 2014, **244**, 27–32.
19 K. K. Huang, X. F. Chu, L. Yuan, W. C. Feng, X. F. Wu, X. Y. Wang and S. H. Feng, *Chem. Commun.*, 2014, **50**, 9200–9203.
20 K. K. Huang, W. C. Feng, L. Yuan, J. X. Zhang, X. F. Chu, C. M. Hou, X. F. Wu and S. H. Feng, *CrystEngComm*, 2014, **16**, 9842–9846.
21 L. Jiang, Y. Zhao and J. Zhai, *Angew. Chem.*, 2004, **116**, 4438–4441.
22 H. C. Zeng, *J. Mater. Chem.*, 2011, **21**, 7511–7526.
23 D. C. Hong, Y. Yamada, T. Nagatomi, Y. Takai and S. Fukuzumi, *J. Am. Chem. Soc.*, 2012, **134**, 19572–19575.
24 J. Feng and F. Heinz, *Energy Environ. Sci.*, 2010, **3**, 1018–1027.
25 X. Li, S. S. S. Fang, J. Teo, Y. L. Foo, A. Borgna, M. Lin and Z. Y. Zhong, *ACS Catal.*, 2012, **2**, 360–369.
26 Z. Omid, J. A. Beardslee and H. Thomas, *J. Phys. Chem. C*, 2014, **118**, 16494–16503.
27 D. M. Robinson, Y. B. Go, M. Mui, G. Gardner, Z. J. Zhang, D. Mastrogiovanni, E. Garfunkel, J. Li, M. Greenblatt and G. C. Dismukes, *J. Am. Chem. Soc.*, 2013, **135**, 3494–3501.
28 C. Zener, *Phys. Rev.*, 1951, **82**, 403–405.
29 X. Wang, F. L. Yuan, P. Hu, L. J. Yu and L. Y. Bai, *J. Phys. Chem. C*, 2008, **112**, 8773–8778.